ADVANCED OPTICAL MATERIALS
www.advopticalmat.de

Impacts of the Lattice Strain on Light Emission in Layered Perovskite Thin flakes

Zhonglong Zhang, Runhui Zhou, Meili Li, Yan-Fang Zhang, Yepei Mo, Yang Yu, Zhangsheng Xu, Boning Sun, Wenqiang Wu, Qiuchun Lu, Nan Lu, Jin Xie, Xiaoming Mo, Shixuan Du, and Caofeng Pan**

Strain engineering, as a non-chemical tuning knob, can enhance the performance of semiconductor devices. Here, an efficient manipulation of light emission is revealed in thin-layered 2D perovskite strongly correlated to layer numbers of $[PbI_6]^{4-}$ octahedron (n) and $[C_6H_5(CH_2)_2NH_3]_2(CH_3NH_3)_{n-1}Pb_nI_{3n+1}$ (N) by applying uniaxial strains (ε) via bending the flexible substrate. As $<n>$ increases from 1 to 3, an efficient light emission redshift (ε from −0.97% to 0.97%) is observed from bandgap shrinkage, and the shrinkage rate increases from 1.97 to 10.38 meV/%, which is attributed to the predominant uniaxial intralayer deformation due to the anisotropy of the $[PbI_6]^{4-}$ octahedron lattice strain. Conversely, as $<N>$ increases from 7 to 48 for $n = 3$, the deformation related to bandgap shrinkage rate is more prominent in small-N flakes ($<N> \approx 7$, 15.2 meV/%) but is easily offset in large-N flakes ($<N> \approx 48$, 7.7 meV/%). This anisotropic lattice deformation, meanwhile, inevitably modulates the carrier recombination dynamics of $[C_6H_5(CH_2)_2NH_3]_2(CH_3NH_3)_{n-1}Pb_nI_{3n+1}$, which is essential for the development of highly efficient photoelectronic devices.

1. Introduction

Future displays should be bendable, stretchable, and wearable to meet consumer demands for portable devices.[1–4] As a critical component of flexible displays, photodetectors, light-emitting diodes, and lasers determine the luminance, definition, color gamut, and saturation of display panels.[5–10] Thus, the development of exceptional optoelectronic devices is urgently needed to meet these requirements. However, the performance of flexible devices is highly dependent on photoactive materials, which must possess high photoelectronic conversion efficiency and mechanical conformability.[11–15] Therefore, it is crucial to explore the mechanical properties of photoactive materials and understand the failure mechanisms under strain, both of which are crucial for designing excellent flexible devices.[16–23]

Metal–halide perovskite single-crystal $APbX_3$ [A: $CH_3NH_3^+$, $HC(NH_2)_2^+$, Cs^+] exhibit low defect density ($\leq 10^{10}$ cm^{-3}, comparable to conventional semiconductors such as crystalline silicon), large optical absorption coefficient ($\geq 10^4$ cm^{-1}), long carrier diffusion length ($\geq$ 10 μm), giant oscillator strength, as well as facile synthesis.[24–26] In particular, the low elastic modulus ($E \approx$ 10–20 GPa) and high mechanical robustness of halide perovskites render their photophysical properties strongly dependent on the strain response of the $[PbX_6]^{4-}$ octahedron lattice, which is a promising flexible

Z. Zhang, Y. Yu, B. Sun, Q. Lu, X. Mo, C. Pan
Center on Nanoenergy Research, Institute of Science and Technology for Carbon Peak & Neutrality; Key Laboratory of Blue Energy and Systems Integration (Guangxi University), Education Department of Guangxi Zhuang Autonomous Region; School of Physical Science & Technology Guangxi University
Nanning 530004, P. R. China
E-mail: pancaofeng@buaa.edu.cn

Z. Zhang, R. Zhou, M. Li, Y. Mo, Y. Yu, Z. Xu, B. Sun, W. Wu, Q. Lu, N. Lu, C. Pan
Beijing Institute of Nanoenergy and Nanosystems
Chinese Academy of Sciences
Beijing 101400, P. R. China
E-mail: 1806386414@pku.edu.cn

Y.-F. Zhang, S. Du
Institute of Physics & University of Chinese Academy of Sciences
Chinese Academy of Sciences
Beijing 100190, P. R. China

W. Wu, C. Pan
Institute of Atomic Manufacturing
Beihang University
Beijing 100191, P. R. China

J. Xie
State Key Laboratory for Mesoscopic Physics, Frontiers Science Centre for Nano-optoelectronics, School of Physics
Peking University
Beijing 100871, P. R. China

S. Du
Songshan Lake Materials Laboratory
Dongguan 523808, P. R. China

The ORCID identification number(s) for the author(s) of this article can be found under https://doi.org/10.1002/adom.202401565

DOI: 10.1002/adom.202401565

optoelectronic component.[27] Therefore, pressure/strain-induced octahedral tilting and lattice distortion in the Pb-X bond length and Pb-X-Pb bond angle fundamentally modulate the bandgap and carrier dynamics of halide perovskites.[28–29] However, recent efforts have mainly focused on halide perovskite polycrystalline materials, and the brittleness and mechanical compatibility of single crystals for uniaxial-strain response devices have rarely been reported, particularly for 2D halide perovskites.[28–31] Indeed, 2D perovskites possess better environmental stability and ductility (E < 10 GPa) than their 3D counterparts,[16,32–33] which has attracted increasing attention for the development of miniaturized high-pressure responsive devices.[34–36] They exhibit interlayer and intralayer compression-dependent lattice deformation and electronic structure evolution behaviors that differ from those of 3D halide perovskites,[37–41] which are yet to be well explored under uniaxial strain.

Herein, we extensively studied the light emission properties of the lattice strain manipulation of 2D perovskite single-crystal (2DPSC) thin flakes of $[C_6H_5(CH_2)_2NH_3]_2(CH_3NH_3)_{n-1}Pb_nI_{3n+1}$ by applying uniaxial strain by bending the flexible substrate. The lattice deformation dynamics and bandgap modulation associated with the <n> and <N> of 2DPSC thin flakes were extensively investigated through optical spectroscopy and first-principles calculations. When $n \geq 3$ ($N \leq 7$), the anisotropic lattice strain of $[Pb_3I_{10}]^{4-}$ led to enhanced uniaxial intralayer deformation, resulting in an optically modulated bandgap range of 24 meV. Conversely, the bandgap shrinkage rate for $N \geq 48$ (7.7 meV/%) was significantly lower compared to that for $N \leq 7$ (15.2 meV/%) for $[C_6H_5(CH_2)_2NH_3]_2(CH_3NH_3)_2Pb_3I_{10}$ ($n = 3$), which was attributed to the effective compensation of the large-N flakes to the uniaxial intralayer deformation. Furthermore, the carrier dynamics induced by uniaxial bending strains were explored through state density, excitation power-dependent spectroscopy, and time-resolved photoluminescence (TRPL) spectroscopy, which demonstrated the atomic-scale relationships between the structure, optical bandgap, and carrier recombination dynamics. This study provides important data for advancing the development of high-performance flexible optoelectronic devices.

2. Results and Discussion

The 2DPSC films of $[C_6H_5(CH_2)_2NH_3]_2(CH_3NH_3)_{n-1}Pb_nI_{3n+1}$ (for n = 1, 2, and 3) were synthesized using a space-confined solution growth technique (more details can be found in Note S1, Supporting Information); a schematic representation of the growth process is illustrated in Figure S1a (Supporting Information). The prepared 2DPSC films with different n values all exhibited smooth, flat, and crack-free surfaces, as illustrated in Figure S2 (Supporting Information). Additionally, the results of the atomic force microscope (AFM) analysis presented in Figure S3 (Supporting Information) demonstrate that the surfaces of 2DPSC films all possess rather low roughness. Pure-phase 2DPSC thin flakes with controllable thickness (20–200 nm) could be produced by mechanical exfoliation owing to the weak van der Waals interactions linking the organic chains between the Ruddlesden–Popper perovskite layers[33,41–42] (**Figure 1a**; Figure S1b, Supporting Information). Optical images of the exfoliated thin flakes (n = 2), along with their corresponding fluorescence images (excited at 395 nm), are presented in Figure 1b and indicate a smooth surface and uniform fluorescence emission. The AFM height profile confirmed the uniform thickness of the exfoliated flakes, demonstrating a thickness of ≈80 nm (Figure 1c). Furthermore, the X-ray diffraction (XRD) patterns of the 2DPSC thin flakes for n = 1, 2, and 3 are shown in Figure 1d to validate the phase purity of the exfoliated flakes at the lattice structure level. The observed diffraction peaks are in good agreement with previous reports,[43–44] validating the lattice structure and high phase purity. Moreover, the pronounced (0K0) peaks for n > 1 indicate a predominant orientation along the [101] direction. Finally, the optical properties of the exfoliated flakes were characterized and validated by spectral analysis. The absorption spectra (Figure 1e) and photoluminescence (PL) spectra (Figure 1f) of the 2DPSC thin flakes for n = 1, 2, and 3 were recorded at room temperature, with absorption edges at 518, 556, and 598 nm and PL peaks at 526, 574, and 622 nm, corresponding to full width at half maximum (FWHM) values of 16, 23, and 28 nm, respectively. These values are consistent with previous reports,[33,41–42] further confirming the high purity of the 2DPSC phase.

The uniaxial strain was applied to the flakes using a flexible substrate to investigate the influence of the lattice strain on the light emission behavior of the exfoliated flakes. As shown in **Figure 2a**, the 2DPSC was transferred to the center of a circular PEN substrate (diameter = 1.5 cm, thickness = 150 µm) and fixed with polymethyl methacrylate, followed by the coating of 10 nm aluminum oxide for enhanced photostability (Figure S4, Supporting Information) via atomic layer deposition. The lower part of Figure 2a illustrates the strain imposition model, where the central angle formed by the bending of the substrate was denoted as θ and the thickness and length of the PEN substrate were denoted as d and L, respectively. The applied strain ε% could be calculated as follows: $\varepsilon\% = \pi \times \theta \times d / 180 \times L$ (for the detailed strain calculation method, refer to Note S1, Supporting Information). A physical image of the strain imposition setup is shown in Figure S5 (Supporting Information).

Uniaxial strains were then applied to the 2DPSC by bending the PEN substrate through a 1D displacement stage, and the PL spectra of samples with the same thickness (40 nm) (Figure S6, Supporting Information) of n = 1, 2, and 3 under strains are depicted in Figure 2b. The PL peak positions evidently redshifted when applied strains changed from compressive strain (ε = −0.97%) to tensile strain (ε = 0.97%), indicating a shrinking of the bandgap. This trend is in good agreement with the previously reported spectral behaviors of both 3D perovskite single crystals and 2D materials under uniaxial strains.[45–51] Notably, the PL peak of $[C_6H_5(CH_2)_2NH_3]_2(CH_3NH_3)_2Pb_3I_{10}$ ($n = 3$) exhibited a significant redshift from 619.1 to 624.2 nm when applied strain varied from −0.97 to 0.97%, which was significantly larger than the redshift observed for n = 2 (573.7 to 575.7 nm) and n = 1 (523.9 to 524.6 nm) under similar conditions (Figure 2b; Figure S7a, Supporting Information). The corresponding optical bandgap (E_g) can be obtained from the PL peak position (λ) using the conversion formula: $E_g = hc/\lambda$, where h is Planck's constant and c is the speed of light. This suggests that the bandgap modulation in n = 3 under strains was more pronounced, reaching up to 10.38 meV/%, comparable to that observed in 3D perovskite single crystals under uniaxial strains but significantly lower than that in 2D materials (1/3). The geometric structures of three

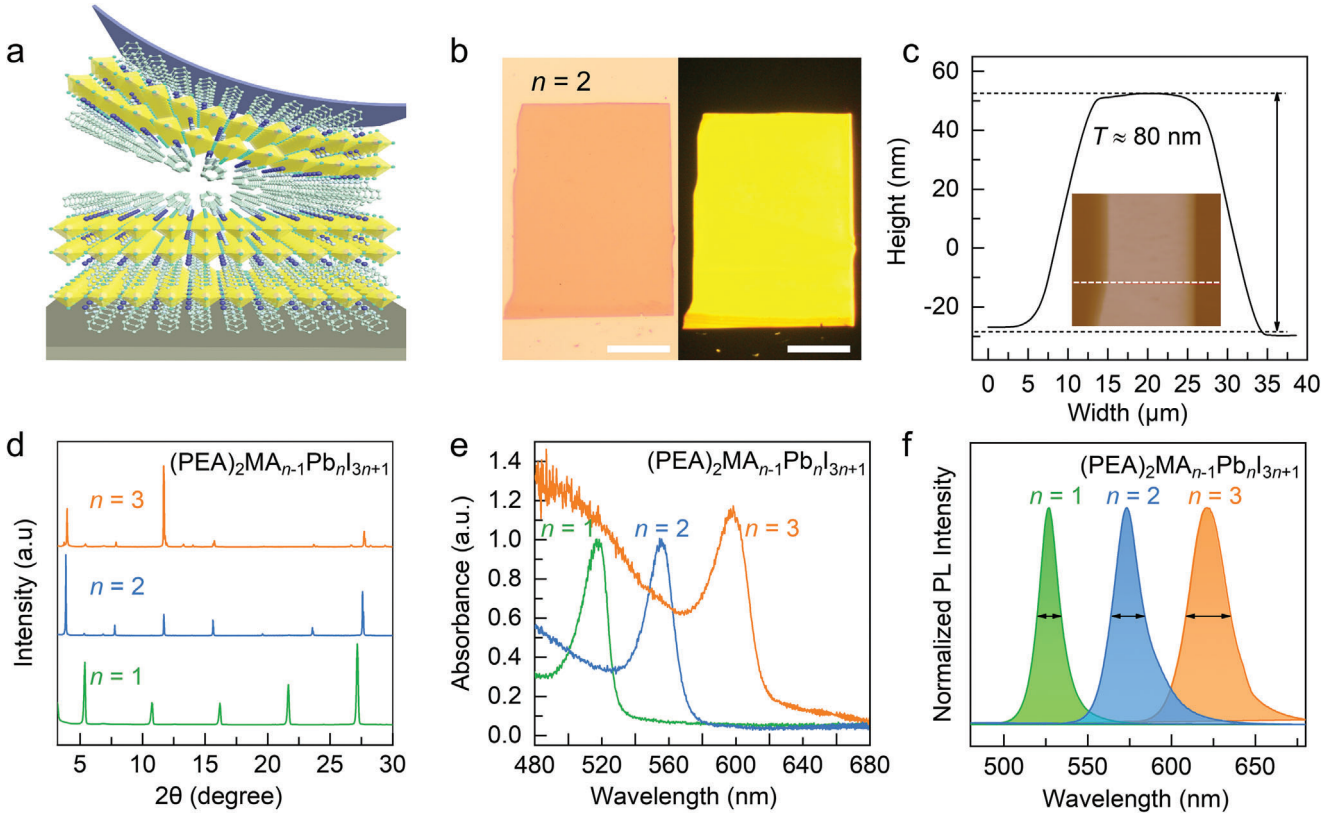

Figure 1. Structural and optical characterization of 2D perovskite single crystals (2DPSCs) of $[C_6H_5(CH_2)_2NH_3]_2(CH_3NH_3)_{n-1}Pb_nI_{3n+1}$. a) Schematic illustration of the exfoliation of 2DPSC ($n = 2$). b) Optical image of a 2DPSC ($n = 2$) thin flake with the corresponding fluorescence image excited by 395 nm (scale bar: 50 μm). c) AFM height profile of the 2DPSC ($n = 2$) thin flake with an AFM optical image (inset). d) XRD spectra of 2DPSC thin flakes with $n = 1$, 2, and 3 from bottom to top, respectively. e) Absorption and f) PL spectra of 2DPSC thin flakes for $n = 1$, 2, and 3 at room temperature.

2DPSCs ($n = 1$, 2, and 3) were constructed (Figure 2c) to investigate the reasons for the different bandgap modulation rates at different n values. The periodicity perpendicular to the 2D perovskite layer is 16.4, 22.8, and 29.2 Å, respectively. Therefore, the corresponding numbers of 2DPSC layers (N) for $n = 1$, 2, and 3, with a thickness of ≈40 nm, were calculated as 24, 17, and 13, respectively (Figure 2d). The relative proportions of the lead halide octahedral and organic layers in the selected samples were calculated and are shown in the upper part of Figure 2e. The results revealed that for $n = 1$, 2, and 3, the structural proportions of the lead halide octahedron were 38, 54, and 62%, respectively. In contrast, the proportions of organic layers followed the opposite trend, at 62, 46, and 38%, respectively. Furthermore, the total peak shifts ($\Delta\lambda$) for $n = 1$, 2, and 3 were calculated to be 0.67, 2.02, and 5.1 nm, respectively, as shown in the lower part of Figure 2e; this demonstrated that the total peak shift was proportional to the proportion of octahedral layers under strain. Consequently, an increase in n can lead to more pronounced uniaxial intra-layer interactions under strain, resulting in a more pronounced modification of the bandgap at a constant thickness.

To further explore the influence of intra- and interlayer interactions on the modulation of the bandgap, we prepared 2DPSC thin flakes (n = 1–3) with different layer numbers (N) (Figure S7b, Supporting Information). **Figure** 3a–d illustrates the N dependence of the PL spectra of the 2DPSC thin flakes ($n = 3$). As depicted in Figure 3a, the most significant PL peak shift under strains was observed for 2DPSC thin flakes ($n = 3$) when $\langle N \rangle \approx 7$, with a redshift from 617.2 (at $\varepsilon = -0.79\%$) to 624.6 nm (at $\varepsilon = 0.79\%$). Correspondingly, for $\langle N \rangle \approx 13$, the PL peak of 2DPSC thin flakes ($n = 3$) shifted from 619.1 (at $\varepsilon = -0.97\%$) to 624.2 nm (at $\varepsilon = 0.97\%$); for $\langle N \rangle \approx 31$, the shift was from 618.5 nm (at $\varepsilon = -0.79\%$) to 622.6 nm (at $\varepsilon = 0.79\%$); and for $\langle N \rangle \approx 48$, the smallest shift was recorded, from 619.2 (at $\varepsilon = -0.79\%$) to 623 nm (at $\varepsilon = 0.79\%$) (Figure 3b–d). For 2DPSC thin flakes ($n = 3$) with layer counts of $\langle N \rangle \approx 7$, 13, 31, and 48, the total peak shifts ($\Delta\lambda$) were 7.4, 5.1, 4.3, and 3.8 nm, respectively, and the corresponding bandgap modulation rates were 15.2, 10.38, 8.8, and 7.7 meV/%, respectively (Figure 3e). For the 2DPSC, thin flakes ($n = 2$) with different layer counts ($\langle N \rangle \approx 9$, 17, 39, 63) exhibited similar trends (Figures S8, S9, Supporting Information). Consequently, considering the interlayer slippage that occurs in samples with higher layer numbers (N) owing to weak van der Waals forces,[52–53] we deem that the increase in the layer number (N) attenuates the uniaxial intralayer interactions under strain, leading to a reduced rate of bandgap modulation at a constant n.

To elucidate the mechanism underlying the strain-modulated bandgap, the electronic structures of the 2DPSCs under strain were examined through first-principles calculations based on the density of functional theory. The partial charge densities of the conduction and valence bands (**Figure** 4a) indicated that the

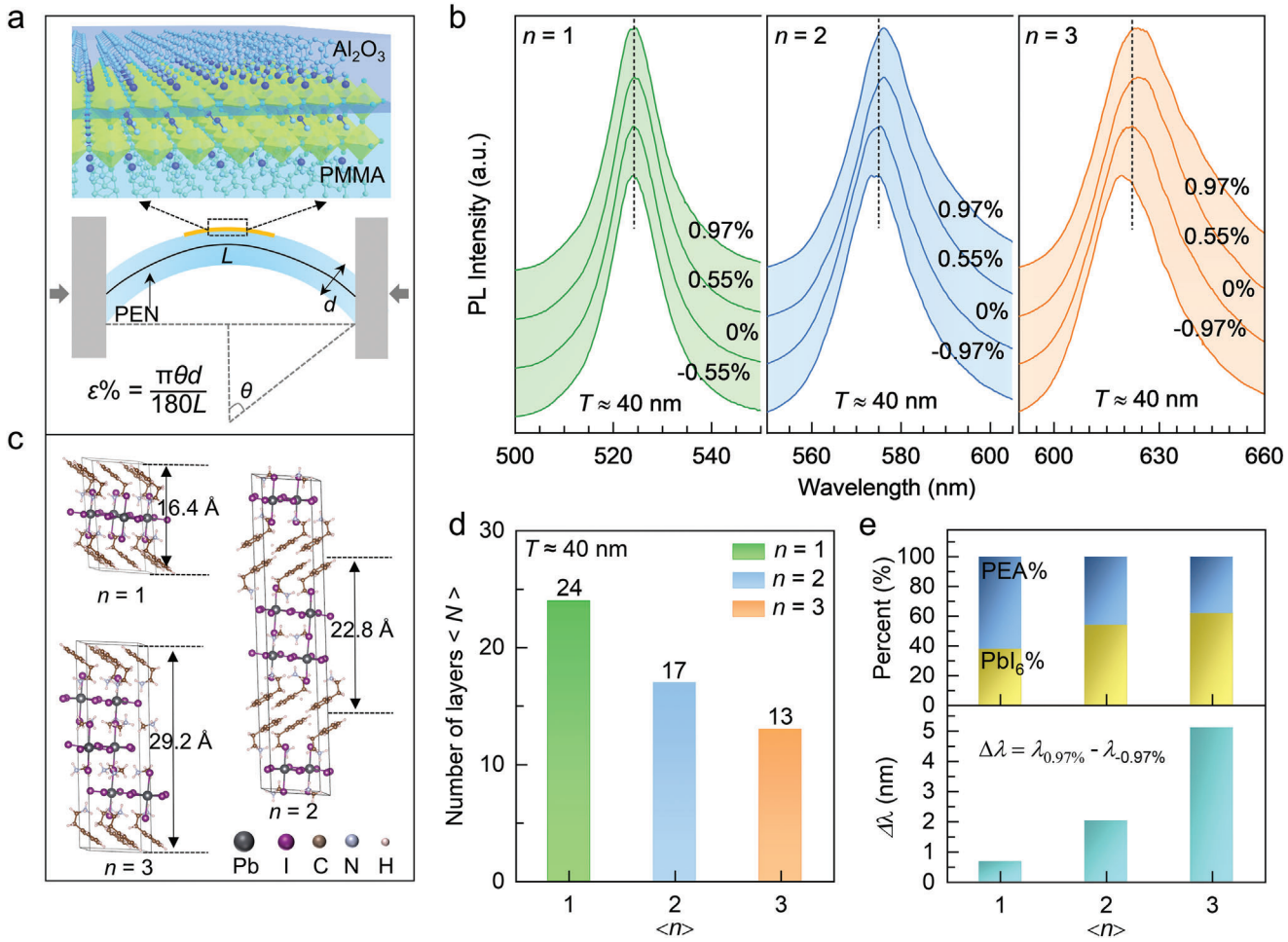

Figure 2. Spectral analysis of strained 2DPSC thin flakes with varying *n* values at a consistent thickness. a) Schematic of strain application. b) PL spectra of 2DPSC thin flakes with varying *n*-values under strains. c) Crystal structures of 2DPSC with varying *n* values. d) Number of layers (*N*) of 2DPSC thin flakes for varying *n* values at $T \approx 40$ nm. e) Total peak shifts ($\Delta\lambda$) (lower panel) and the ratio of organic to inorganic layers (upper panel) correspond to different *n* values of 2DPSC thin flakes.

electronic states close to the Fermi level were mainly contributed by the Pb and I atoms rather than by the organic sheet, which was further emphasized by the projected density of states (DOS, Figure S10, Supporting Information). The energy band structure for $n = 3$ under −1.13%, 0%, and 1.13% strains is depicted in Figure 4b, with a direct bandgap observed at the Γ point under all strain conditions. Under compressive strain ($\varepsilon = -1.13\%$), the bandgap increased to 1.768 eV, contrasting with the value of 1.760 eV observed in the strain-free state ($\varepsilon = 0\%$). Conversely, the bandgap decreased to 1.714 eV under tensile strain ($\varepsilon = 1.13\%$). The bandgap variation behavior was concordant with the observed redshift under tensile strain and blueshift under compressive strain in the measured PL spectra. Meanwhile, the conduction band minimum (CBM), which is dominated by Pb 6*p* orbitals, underwent an energy reduction from compressive to tensile strains. In contrast, the valence band maximum (VBM), predominantly associated with I 5*s* orbitals, exhibited a smaller energy change attributable to the dumbbell-shaped *p* orbitals, which are more susceptible to lattice strain than symmetric *s* orbitals.

Similar trends were observed for the $n = 2$ thin flakes of 2DPSC under −1.13, 0, and 1.13% strains (Figure S11, Supporting Information). The variation in the bandgap as a function of strain is shown in Figure 4c; this illustrates that the bandgap of $[C_6H_5(CH_2)_2NH_3]_2(CH_3NH_3)_{n-1}Pb_nI_{3n+1}$ gradually decreased when the applied strain changed from compressive to tensile. In addition, the change in the bandgap was more significant for $n = 3$ ($\Delta E = 53.1$ meV) than that for $n = 2$ ($\Delta E = 46.6$ meV). These findings are generally consistent with the experimental observations of the PL spectra. Therefore, the results of the first principles calculations confirmed that the modulation of the bandgap resulted from the anisotropic deformation of the octahedral formation of Pb-I by the applied uniaxial strain, suggesting that the deformation of the crystal structure led to a redistribution of the electronic structure. These results provide a theoretical basis for understanding the bandgap modulation influenced by <*n*> and <*N*>.

The ε dependence of Raman spectra was further performed to probe the lattice strain of 2DPSC thin flakes (Figure 4d–f). As

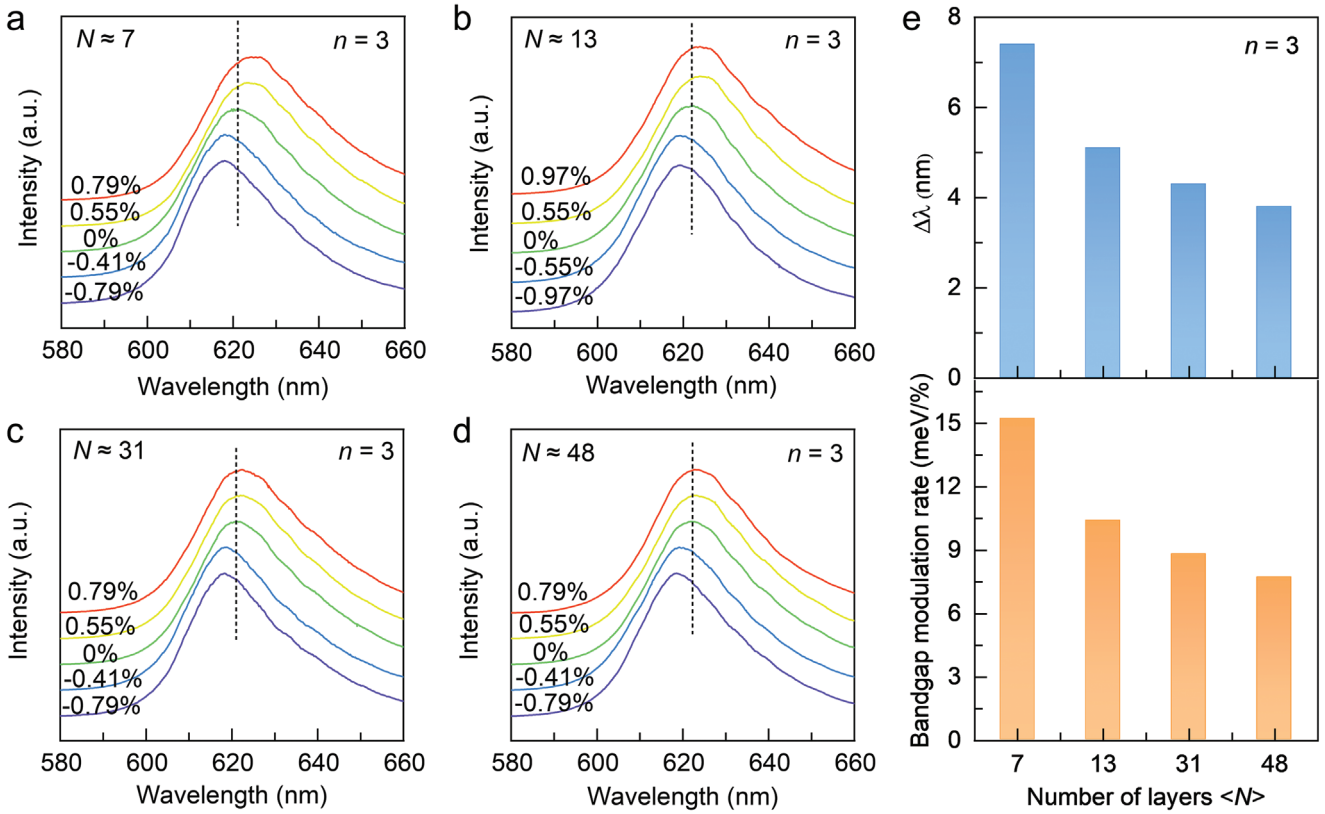

Figure 3. Strain-dependent spectral modulation of 2DPSC thin flakes with different numbers of layers (N) when $n = 3$. a) PL spectra under strains for 2DPSC thin flakes ($n = 3$) with $\langle N \rangle \approx 7$, b) $\langle N \rangle \approx 13$, c) $\langle N \rangle \approx 31$, and d) $\langle N \rangle \approx 48$. e) Strain-modulated total peak shifts ($\Delta\lambda$) (upper panel) with corresponding band gap modulation rates (lower panel) for 2DPSC thin flakes with different numbers of layers (N).

shown in Figure 4d, Raman peaks were clearly observed at ≈90 cm^{-1}, which corresponded to the stretching vibrational mode of the Pb-I bond.[54–55] Owing to compressive strain ($\varepsilon = -0.55\%$), the Raman peak shifted to a higher frequency due to bond shortening, while at tensile strain ($\varepsilon = 0.79\%$), it shifted to lower frequencies due to bond stretching; this trend was also observed for other 2DPSC thin flakes with varying $\langle n \rangle$ and $\langle N \rangle$ (Figure S12, Supporting Information). For 2DPSC thin flakes of the same thickness ($T \approx 20$ nm), the slopes of the linear fit of the Raman peak position variations for $n = 1$, 2, and 3 were 0.23, 1.7, and 2.02, respectively (Figure 4e). The observed values indicate that the displacement of the Raman peaks associated with the lead–halide octahedron accelerates with increasing n-values. This observation suggests that 2DPSC thin flakes with larger n values undergo greater Pb-I stretching under the same strain, resulting in a more pronounced uniaxial intralayer deformation of the lead–halide octahedron. The minimal lattice strain for $n = 1$ was ascribed not only to the inorganic octahedral structure but also to the distorted structure of the sample,[31,56] rendering it insensitive to mechanical strains.

Moreover, for a given $\langle n \rangle$ ($n = 3$), the slopes of the linear fit of the changes in Raman peak positions for $\langle N \rangle \approx 7$, 13, and 21 were 2.02, 1.6, and 1.4, respectively (Figure 4f). In addition, the Raman peak shifts exhibited a consistent pattern at $n = 2$ (Figure S13, Supporting Information). The slope of the linear fitting for the Raman peak position decreased as the number of 2DPSC layers (N) increased, indicating a deceleration of the peak shift. This observation suggests that samples with a larger number of 2DPSC layers (N) exhibit less Pb-I stretching at the same strain, resulting in an offset of the uniaxial intralayer deformation of the lead–halide octahedron. In summary, Raman spectroscopy offers valuable insights into the mechanisms of bandgap modulation, focusing on the influence of lattice strain. An increase in the number of lead–halide octahedron layers (n) leads to greater anisotropic deformation of the octahedron under strain, whereas a higher number of 2DPSC layers (N) mitigates the uniaxial intralayer deformation in the lattice.

We further explored the dynamics of photogenerated carrier recombination under strains because lattice distortion typically modifies the bandgap, which can influence the process of carrier recombination.[28,57–59] For 2DPSC thin flakes with the same thickness ($T \approx 40$ nm), the PL integral area for $n = 1$, 2, and 3 increased by factors of 1.3, 2.6, and 1.7, respectively (ε from −0.97% to 0.97%) (Figure S14 and Table S1, Supporting Information). Furthermore, under tensile strain ($\varepsilon = 1.13\%$), the DOS peak near the valence band of $[C_6H_5(CH_2)_2NH_3]_2(CH_3NH_3)_2Pb_3I_{10}$ was wider compared with those at 0 and −1.13% strains (Figure S10, Supporting Information); this is attributed to the increased spatial overlap of the electron and hole wave functions (**Figure 5a**; Figure S15, Supporting Information) at higher tensile strains, composed of the respective Pb 6p and I 5s orbitals. This spatial overlap enhancement is likely contributed to the

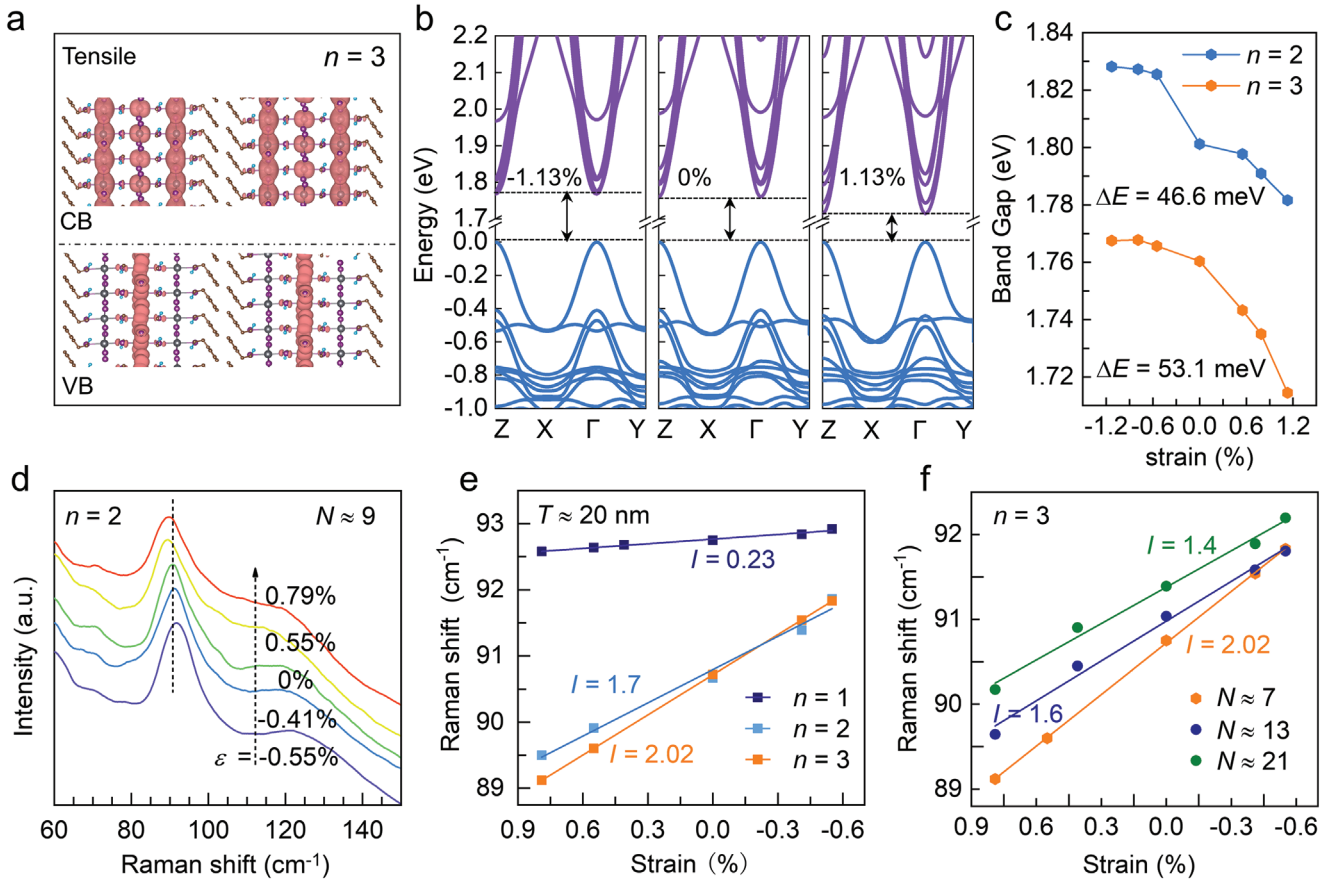

Figure 4. Theoretical calculations and Raman spectral verification of 2DPSC thin flakes under strains. a) Partial charge densities of the conduction band and valence band close to the Fermi level, integrated from −0.6 eV to the E_F and from the E_F to 2.0 eV under tensile strain ($n = 3$). b) Plot of the energy band structure from left to right, corresponding to −1.13, 0, and 1.13% strains ($n = 3$). c) Theoretically calculated plots of bandgap energy differences with strains corresponding to $n = 2$ and 3. d) Raman spectra of 2DPSC thin flake ($n = 2$, $\langle N \rangle \approx 9$) at different strains. e) Raman peak positions versus strains for the same thickness ($T \approx 20$ nm) with $n = 1$, 2, and 3 respectively. f) Raman peak position versus strain curves for the same n value ($n = 3$) with $\langle N \rangle \approx 7$, 13, and 21, respectively.

strain-induced distortion of the lead–halide octahedron, which results in the displacement of Pb and I atoms, thereby exciting high-energy phonon modes associated with the organic sublattice.[59] In addition, this spatial overlap enhancement typically results in an increased recombination rate,[28,59] thereby enhancing the PL emission.

We further investigated the radiative states of the 2DPSC thin flakes under strain for different n values using power-dependent excited-state dynamics.[60–61] Excitation power-dependent PL spectra were collected in situ as the strains varied from −0.79 to 0.79% for the aforementioned 2DPSC thin flakes ($n = 1$, 2, and 3) (Figure S16, Supporting Information). Correspondingly, the PL spectra exhibited a gradual increase in intensity as the excitation power increased, indicating a pronounced power dependence. The integral PL intensity (I) was found to be correlated with the excitation power (P), following an exponential function, $I \propto P^k$. Here, the recombination coefficients (k) 1 and 2 correspond to monomolecular and bimolecular recombination processes, respectively.[60–61] For strain-free conditions, the recombination coefficient "k" for the $n = 1$, 2, and 3 fits was between 1 and 2 (Figure 5b), suggesting the coexistence of recombination processes involving excitons and free carriers. Moreover, the carrier recombination coefficient (k) increased with $\langle n \rangle$, suggesting a decrease in the proportion of exciton recombination and an increase in the proportion of free carrier recombination, which might be influenced by the decrease in exciton binding energy with $\langle n \rangle$.[33,42] The recombination coefficients (k) post-straining for the 2DPSC thin flakes with $n = 1$, 2, and 3 are presented in Figure S17 (Supporting Information). The values of k for $n = 1$ increased from 1.04 to 1.12 as the strains varied from −0.55% to 0.79%. Similarly, these k values increased from 1.18 and 1.32 to 1.46 and 1.81 for $n = 2$ and 3, respectively. The summary plot of k values as a function of ε suggests that the proportion of exciton recombination increases under tensile strain and decreases under compressive strain (Figure 5c). Thus, the increase in the proportion of exciton recombination within the 2DPSC thin flakes under tensile strain further reinforces the reason for the enhanced PL emission.

Finally, we investigated the PL decay dynamics of 2DPSC thin flakes under strain for different n values using TRPL spectroscopy. For strain-free conditions, the TRPL curves for $n = 1$, 2, and 3 depicted in Figure 5d deviate from the single exponential

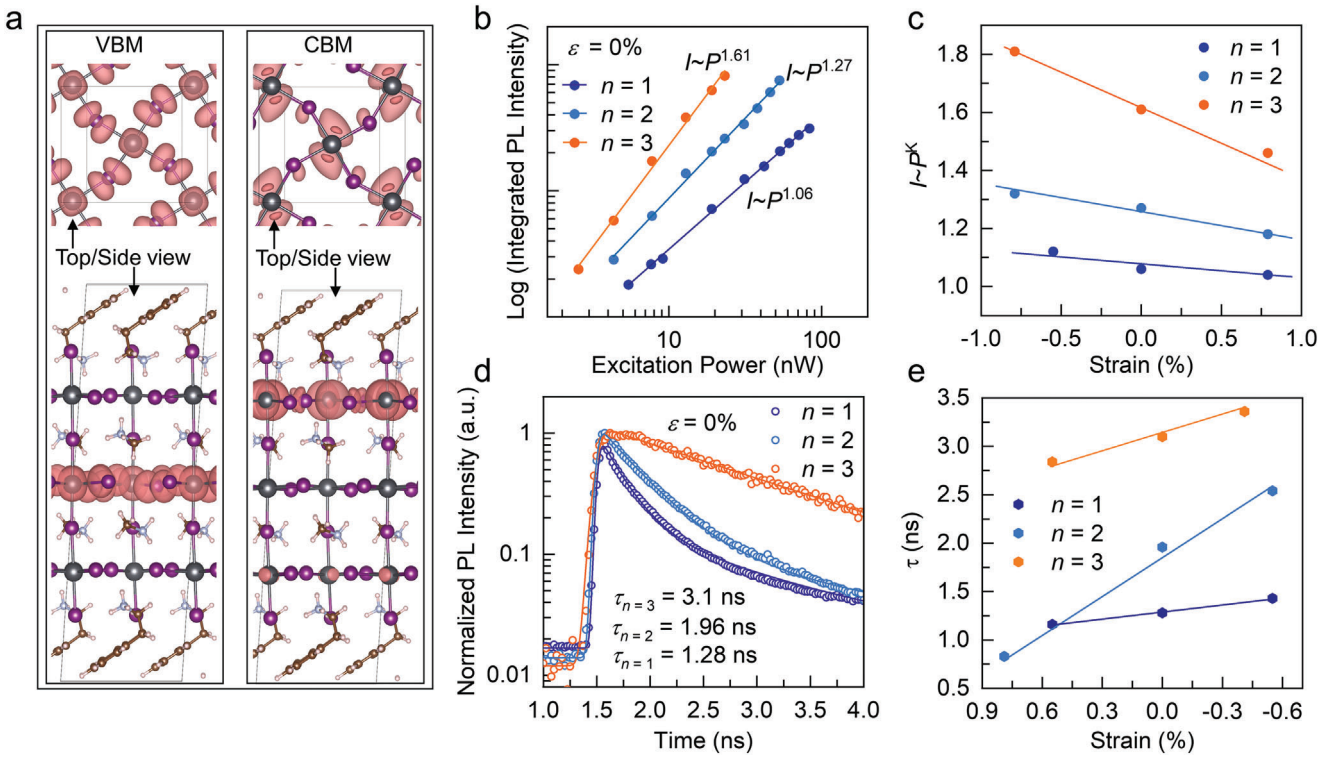

Figure 5. Carrier recombination dynamics analysis of 2DPSC thin flakes under strains. a) Band decomposed charge densities of the VBM (left) and CBM (right) in the top view and side view at a tensile strain of 1.13%, respectively ($n = 3$). b) Logarithmic plots of the integral PL intensity versus excitation power for $n = 1$, 2, and 3, respectively. c) Curves of the recombination coefficient "k" versus strains for $n = 1$, 2, and 3, respectively. d) TRPL spectra for $n = 1$, 2, and 3, respectively. e) Fitted carrier lifetimes of the corresponding TPRL spectra at different strains for $n = 1$, 2, and 3, respectively.

behavior typical for exciton recombination as n increases.[62–63] By fitting the TRPL lifetimes with a bi-exponential function (Note S1, Supporting Information), the carrier lifetimes (τ) for $n = 1$, 2, and 3 were determined to be 1.28, 1.96, and 3.1, respectively (Figure 5d). The longer carrier lifetime at $n = 3$ is attributed to the higher proportion of free carrier recombination, which is consistent with the excitation power-dependent PL results. The TRPL spectra post-straining for the 2DPSC thin flakes with $n = 1$, 2, and 3 are shown in Figure S18 (Supporting Information). Evidently, the fitted carrier lifetimes for $n = 1$ decreased from 1.43 to 1.16 ns as the strains varied from −0.55 to 0.55%. Similarly, the fitted carrier lifetimes decreased from 2.84 and 3.36 ns to 0.83 and 2.54 ns for $n = 2$ and 3, respectively (Figure 5e); this suggests that an increase in the proportion of exciton recombination induced by tensile strain enhances the carrier recombination rate, thereby shortening the carrier lifetime. Thus, the study of carrier recombination dynamics under uniaxial strain reveals that anisotropic lattice deformation not only shifts the bandgap but also modifies the spatial overlap of electron-hole wave functions, thereby enhancing the PL emission rate.

3. Conclusion

We systematically elucidated the light emission properties of lattice strain manipulation in $[C_6H_5(CH_2)_2NH_3]_2(CH_3NH_3)_{n-1}Pb_nI_{3n+1}$ ($n = 1$, 2, and 3) thin flakes by applying uniaxial strains by bending a flexible substrate. For the 2DPSC thin flakes with the same thickness under strains, the uniaxial intralayer deformation of the lead halide octahedron increased with n values. As <n> increased from 1 to 3, the bandgap shrinkage rate increased from 1.97 to 10.38 meV/% (ε from −0.97 to 0.97%), which was attributed to the anisotropic lattice strain of the lead halide octahedron, which dominates the uniaxial intralayer deformation. Furthermore, for 2DPSC thin flakes with the same n value under strains, the uniaxial intralayer deformation of the lead halide octahedron decreased with <N>. As <N> increased from 7 to 48 ($n = 3$), the bandgap shrinkage rate decreased from 15.2 to 7.7 meV/% (ε from −0.79 to 0.79%). Further experiments and theoretical calculations revealed the relationship between the strain-induced crystal structure and the light emission properties of the 2DPSC thin flakes, which might promote the development of high-performance flexible optoelectronic devices.

Supporting Information

Supporting Information is available from the Wiley Online Library or from the author.

Acknowledgements

Z.L.Z. and R.H.Z. contributed equally to this work. The authors thank the support of the National Natural Science Foundation of China (No. 62105035, 52125205, 52250398, U20A20166, 52192614, and 52003101),

the National Key R&D Program of China (2021YFB3200300), the Natural Science Foundation of Beijing Municipality (2222088), the Shenzhen Science and Technology Program (Grant No. KQTD20170810105439418) and the Fundamental Research Funds for the Central Universities.

Conflict of Interest

The authors declare no conflict of interest.

Data Availability Statement

The data that support the findings of this study are available from the corresponding author upon reasonable request.

Keywords

2D perovskite, bandgap, carrier dynamics, lattice strain, uniaxial strains

Received: June 11, 2024
Revised: August 16, 2024
Published online: August 29, 2024

[1] Z. Zhang, Y. Wang, S. Jia, C. Fan, *Nat. Photonics* **2024**, *18*, 114.
[2] Z. Zhang, W. Wang, Y. Jiang, Y.-X. Wang, Y. Wu, J.-C. Lai, S. Niu, C. Xu, C.-C. Shih, C. Wang, H. Yan, L. Galuska, N. Prine, H.-C. Wu, D. Zhong, G. Chen, N. Matsuhisa, Y. Zheng, Z. Yu, Y. Wang, R. Dauskardt, X. Gu, J. B. H. Tok, Z. Bao, *Nature* **2022**, *603*, 624.
[3] J. Liu, T. Ye, D. Yu, S. Liu, D. Yang, *Angew. Chem., Int. Ed.* **2023**, *62*, 202307225.
[4] Y. Lu, X. Qu, W. Zhao, Y. Ren, W. Si, W. Wang, Q. Wang, W. Huang, X. Dong, *Research* **2020**, *2020*, 2038560.
[5] C. Allard, *Nat. Rev. Mater.* **2022**, *7*, 335.
[6] D. W. Kim, S. W. Kim, G. Lee, J. Yoon, S. Kim, J.-H. Hong, S.-C. Jo, U. Jeong, *Light Sci. Appl.* **2023**, *12*, 61.
[7] C. F. Pan, L. Dong, G. Zhu, S. M. Niu, R. M. Yu, Q. Yang, Y. Liu, Z. L. Wang, *Nat. Photonics* **2013**, *7*, 752.
[8] J. He, R. Wei, S. Ge, W. Wu, J. Guo, J. Tao, R. Wang, C. Wang, C. Pan, *InfoMat* **2024**, *6*, e12493.
[9] W. Wu, H. Lu, X. Han, C. Wang, Z. Xu, S.-T. Han, C. Pan, *Small Methods* **2023**, *7*, 2201499.
[10] Z.-P. He, X. Han, W.-Q. Wu, Z.-S. Xu, C.-F. Pan, *Rare Met.* **2024**, *43*, 1407.
[11] Z. Zhang, *Nat. Rev. Mater.* **2022**, *7*, 839.
[12] M. J. Choi, J. W. Lee, H. W. Jang, *Adv. Mater.* **2023**, *36*, 2308827.
[13] S.-H. Chin, J.-W. Lee, *Nano. Res. Energy* **2023**, *2*, 9120071.
[14] W. Liu, H. Wang, *J. Materiomics* **2020**, *6*, 385.
[15] Y. Zhou, R. Xiong, P. Wang, X. Wu, B. Sa, C. Lin, M. Gao, T. Lin, C. Zhao, *J. Materiomics* **2022**, *8*, 586.
[16] Q. Tu, D. Kim, M. Shyikh, M. G. Kanatzidis, *Matter* **2021**, *4*, 2765.
[17] Q. Zhang, S. Zuo, P. Chen, C. Pan, *InfoMat* **2021**, *3*, 987.
[18] W. Ma, J. Lu, B. Wan, D. Peng, Q. Xu, G. Hu, Y. Peng, C. Pan, Z. L. Wang, *Adv. Mater.* **2020**, *32*, 1905795.
[19] X. Wen, W. Wu, C. Pan, Y. Hu, Q. Yang, Z. L. Wang, *Nano Energy* **2015**, *14*, 276.
[20] Z. Wu, Y. Wang, Y. Dou, L. Zhou, J. Zhu, *Nano. Res. Energy* **2023**, *2*, 9120080.
[21] W. Gao, J. Huang, J. He, R. Zhou, Z. Li, Z. Chen, Y. Zhang, C. Pan, *InfoMat* **2023**, *5*, e12426.
[22] J. Tao, M. Dong, L. Li, C. Wang, J. Li, Y. Liu, R. Bao, C. Pan, *Microsyst. Nanoeng.* **2020**, *6*, 62.
[23] J. G. Maier, A. Gadelmawla, N. H. Khansur, K. G. Webber, *J. Materiomics* **2023**, *9*, 673.
[24] B. R. Sutherland, E. H. Sargent, *Nat. Photonics* **2016**, *10*, 295.
[25] D. Shi, V. Adinolfi, R. Comin, M. Yuan, E. Alarousu, A. Buin, Y. Chen, S. Hoogland, A. Rothenberger, K. Katsiev, Y. Losovyj, X. Zhang, P. A. Dowben, O. F. Mohammed, E. H. Sargent, O. M. Bakr, *Science* **2015**, *347*, 519.
[26] A. J. Ramadan, R. D. J. Oliver, M. B. Johnston, H. J. Snaith, *Nat. Rev. Mater.* **2023**, *8*, 822.
[27] A. Liu, I. S. Mukhin, R. M. Islamova, J. Tian, *Adv. Funct. Mater.* **2024**, *34*, 2312209.
[28] Y. Jiao, S. Yi, H. Wang, B. Li, W. Hao, L. Pan, Y. Shi, X. Li, P. Liu, H. Zhang, C. Gao, J. Zhao, J. Lu, *Adv. Funct. Mater.* **2020**, *31*, 2006243.
[29] L. Gu, D. Li, L. Chao, H. Dong, W. Hui, T. Niu, C. Ran, Y. Xia, L. Song, Y. Chen, W. Huang, *Sol. RRL* **2021**, *5*, 2000672.
[30] B. Yang, D. Bogachuk, J. Suo, L. Wagner, H. Kim, J. Lim, A. Hinsch, G. Boschloo, M. K. Nazeeruddin, A. Hagfeldt, *Chem. Soc. Rev.* **2022**, *51*, 7509.
[31] Q. Tu, I. Spanopoulos, S. Hao, C. Wolverton, M. G. Kanatzidis, G. S. Shekhawat, V. P. Dravid, *ACS Energy Lett.* **2019**, *4*, 796.
[32] I. Spanopoulos, I. Hadar, W. Ke, Q. Tu, M. Chen, H. Tsai, Y. He, G. Shekhawat, V. P. Dravid, M. R. Wasielewski, A. D. Mohite, C. C. Stoumpos, M. G. Kanatzidis, *J. Am. Chem. Soc.* **2019**, *141*, 5518.
[33] H. Gu, J. Xia, C. Liang, Y. Chen, W. Huang, G. Xing, *Nat. Rev. Mater.* **2023**, *8*, 533.
[34] F. Xu, Y. Zou, Y. Dai, M. Li, Z. Li, *Mater. Chem. Front.* **2023**, *7*, 2102.
[35] H. Li, Y. Qin, B. Shan, Y. Shen, F. Ersan, E. Soignard, C. Ataca, S. Tongay, *Adv. Mater.* **2020**, *32*, 1907364.
[36] M.-E. Sun, Y. Wang, F. Wang, J. Feng, L. Wang, H. Gao, G. Chen, J. Gu, Y. Fu, K. Bu, T. Fu, J. Li, X. Lü, L. Jiang, Y. Wu, S.-Q. Zang, *J. Am. Chem. Soc.* **2023**, *145*, 8908.
[37] S. Liu, S. Sun, C. K. Gan, A. G. Del Águila, Y. Fang, J. Xing, T. T. H. Do, T. J. White, H. Li, W. Huang, *Sci. Adv.* **2019**, *5*, eaav9445.
[38] G. Liu, L. Kong, P. Guo, C. C. Stoumpos, Q. Hu, Z. Liu, Z. Cai, D. J. Gosztola, H.-k. Mao, M. G. Kanatzidis, R. D. Schaller, *ACS Energy Lett.* **2017**, *2*, 2518.
[39] D. Liu, Y.-X. Yin, F.-J. Liu, C.-C. Miao, X.-M. Zhuang, Z.-Y. Pang, M.-S. Xu, M. Chen, Z.-X. Yang, *Rare Met.* **2022**, *41*, 1753.
[40] Y. Zhu, Q. Cui, J. Chen, F. Chen, Z. Shi, X. Zhao, C. Xu, *ACS Appl. Mater. Interfaces* **2021**, *13*, 6820.
[41] K. Leng, W. Fu, Y. Liu, M. Chhowalla, K. P. Loh, *Nat. Rev. Mater.* **2020**, *5*, 482.
[42] B. Chen, R. Yu, G. Xing, Y. Wang, W. Wang, Y. Chen, X. Xu, Q. Zhao, *ACS Energy Lett.* **2023**, *9*, 226.
[43] Q. Sun, C. Zhao, Z. Yin, S. Wang, J. Leng, W. Tian, S. Jin, *J. Am. Chem. Soc.* **2021**, *143*, 19128.
[44] X. Chen, H. Lu, Z. Li, Y. Zhai, P. F. Ndione, J. J. Berry, K. Zhu, Y. Yang, M. C. Beard, *ACS Energy Lett.* **2018**, *3*, 2273.
[45] Z. Yang, J. Lu, M. ZhuGe, Y. Cheng, J. Hu, F. Li, S. Qiao, Y. Zhang, G. Hu, Q. Yang, D. Peng, K. Liu, C. Pan, *Adv. Mater.* **2019**, *31*, 1900647.
[46] M. Li, J. Lu, P. Wan, M. Jiang, F. Lin, X. Wu, X. Liu, C. Pan, *Adv. Opt. Mater.* **2023**, *11*, 2202723.
[47] Y. Yu, C.-D. Dong, R. Binder, S. Schumacher, C.-Z. Ning, *ACS Nano* **2023**, *17*, 4230.
[48] Y. Peng, J. Lu, D. Peng, W. Ma, F. Li, Q. Chen, X. Wang, J. Sun, H. Liu, C. Pan, *Adv. Funct. Mater.* **2019**, *29*, 1905051.
[49] W. Ma, J. Lu, Z. Yang, D. Peng, F. Li, Y. Peng, Q. Chen, J. Sun, J. Xi, C. Pan, *ACS Nano* **2019**, *13*, 5049.
[50] J. Lu, Z. Yang, F. Li, M. Jiang, Y. Zhang, J. Sun, G. Hu, Q. Xu, C. Xu, C. Pan, Z. L. Wang, *Mater. Today* **2019**, *24*, 33.
[51] M. Gao, L. Yu, Q. Lv, F. Kang, Z.-H. Huang, R. Lv, *J. Materiomics* **2023**, *9*, 768.
[52] Q. Tu, I. Spanopoulos, P. Yasaei, C. C. Stoumpos, M. G. Kanatzidis, G. S. Shekhawat, V. P. Dravid, *ACS Nano* **2018**, *12*, 10347.

[53] A. Falin, Q. Cai, E. J. G. Santos, D. Scullion, D. Qian, R. Zhang, Z. Yang, S. Huang, K. Watanabe, T. Taniguchi, M. R. Barnett, Y. Chen, R. S. Ruoff, L. H. Li, *Nat. Commun.* **2017**, *8*, 15815.
[54] S. Guo, K. Bu, J. Li, Q. Hu, H. Luo, Y. He, Y. Wu, D. Zhang, Y. Zhao, W. Yang, M. G. Kanatzidis, X. Lü, *J. Am. Chem. Soc.* **2021**, *143*, 2545.
[55] Y. Yin, W. Tian, H. Luo, Y. Gao, T. Zhao, C. Zhao, J. Leng, Q. Sun, J. Tang, P. Wang, Q. Li, X. Lü, J. Bian, S. Jin, *ACS Energy Lett.* **2021**, *7*, 154.
[56] C. C. Stoumpos, D. H. Cao, D. J. Clark, J. Young, J. M. Rondinelli, J. I. Jang, J. T. Hupp, M. G. Kanatzidis, *Chem. Mat.* **2016**, *28*, 2852.
[57] C. Zhu, X. Niu, Y. Fu, N. Li, C. Hu, Y. Chen, X. He, G. Na, P. Liu, H. Zai, Y. Ge, Y. Lu, X. Ke, Y. Bai, S. Yang, P. Chen, Y. Li, M. Sui, L. Zhang, H. Zhou, Q. Chen, *Nat. Commun.* **2019**, *10*, 815.
[58] Q.-L. Lin, Z.-F. Qian, X.-Y. Dai, Y.-L. Sun, R.-H. Wang, *Rare Met.* **2022**, *41*, 1761.
[59] A. Y. Chang, Y. J. Cho, K. C. Chen, C. W. Chen, A. Kinaci, B. T. Diroll, M. J. Wagner, M. K. Y. Chan, H. W. Lin, R. D. Schaller, *Adv. Energy Mater.* **2016**, *6*, 1600422.
[60] H. Dong, C. Zhang, W. Nie, S. Duan, C. N. Saggau, M. Tang, M. Zhu, Y. S. Zhao, L. Ma, O. G. Schmidt, *Angew. Chem., Int. Ed.* **2022**, *61*, 202115875.
[61] H. He, Q. Yu, H. Li, J. Li, J. Si, Y. Jin, N. Wang, J. Wang, J. He, X. Wang, Y. Zhang, Z. Ye, *Nat. Commun.* **2016**, *7*, 10896.
[62] J. Lu, W. Chen, C. Zhou, S. Yang, C. Wang, R. Wang, X. Wang, Z. Gan, B. Jia, X. Wen, *J. Mater. Chem. C* **2021**, *9*, 8966.
[63] J. C. Blancon, H. Tsai, W. Nie, C. C. Stoumpos, L. Pedesseau, C. Katan, M. Kepenekian, C. M. M. Soe, K. Appavoo, M. Y. Sfeir, S. Tretiak, P. M. Ajayan, M. G. Kanatzidis, J. Even, J. J. Crochet, A. D. Mohite, *Science* **2017**, *355*, 1288.